

PAPER

Hollow porous BiOCl microspheres assembled with single layer of nanocrystals: spray solution combustion synthesis and the enhanced photocatalytic properties

To cite this article: Zhongxiang Yang *et al* 2021 *Nanotechnology* **32** 205602

View the [article online](#) for updates and enhancements.

You may also like

- [Two-dimensional ultrathin BiOCl nanosheet/graphene heterojunction with enhanced photocatalytic activity](#)
Meili Guan, Xuan Zhang, Jian Bao *et al.*
- [Synthesis, structure, and photocatalytic activity of PANI/BiOCl nanocomposites](#)
Jie Wang, XiaoYun Hao, YouXiang Jiang *et al.*
- [Easy synthesis of high \(110\) facet-exposed BiOCl microspheres with excellent visible light degradation capability towards RhB](#)
Guilong Xu, Shucheng Liu, Yi Tang *et al.*



ECS
The
Electrochemical
Society
Advancing solid state &
electrochemical science & technology

DISCOVER
how sustainability
intersects with
electrochemistry & solid
state science research

Hollow porous BiOCl microspheres assembled with single layer of nanocrystals: spray solution combustion synthesis and the enhanced photocatalytic properties

Zhongxiang Yang¹, Zhichao Shang¹, Fang Liu², Yirui Chen¹, Xiaohong Wang^{1,*}, Bangsheng Zhang^{1,3} and Guiqing Liu^{1,3}

¹ School of Materials Science and Engineering, China University of Mining and Technology, Xuzhou 221116, People's Republic of China

² Department of Aerial Ammunition Support, Air Force Logistics College, Xuzhou 221116, People's Republic of China

³ Jiangsu BGRIMM Metal Recycling Science and Technology, BGRIMM Technology Group, Xuzhou 221116, People's Republic of China

E-mail: wxhcumt@cumt.edu.cn

Received 11 October 2020, revised 24 January 2021

Accepted for publication 11 February 2021

Published 26 February 2021



CrossMark

Abstract

The hollow porous microspheres assembled with BiOCl nanocrystals were successfully synthesized via a facile spray solution combustion synthesis method. The microstructure, morphology, absorbance, optical properties of the samples were investigated in detail. The results show that hollow porous BiOCl microspheres have narrow band gaps (2.66–2.71 eV), and the degradation rate of rhodamine B (RhB) can reach 98% under visible light irradiation for 60 min. Furthermore, the mechanism of the photocatalytic degradation of RhB was proposed through the experiment of trapping active species. This excellent photocatalytic property can be ascribed to the larger specific surface area and the special microstructure.

Keywords: porosity, combustion synthesis, BiOCl, photocatalysis

(Some figures may appear in colour only in the online journal)

1. Introduction

With the rapid development of worldwide industry and economics, environmental pollution has become one of the biggest global problems in new century [1–3]. Semiconductor photocatalysis technology has a great potential for the degradation of organic pollutants because of its high efficiency, energy saving, and pollution-free [4–6]. Bismuth oxychloride (BiOCl), as one of the important main group multicomponent V–VI–VII semiconductors, has been widely studied due to its outstanding physical and chemical properties in various fields [7, 8]. BiOCl is known to be a tetragonal layered structure containing [Cl–Bi–O–Bi–Cl] sheets with the

Cl atoms along the *c*-axis by nonbonding interactions. The strong internal static electric fields perpendicular to the Cl layer and the bismuth oxide-based fluorite-like layer can reduced the recombination of photogenerated electron–hole pairs [8–10]. And the photogenerated charge carriers can transfer to the surface quickly to react with the organic pollutant molecules [11–16]. These properties indicate that it's a good candidate for photocatalyst.

Many efforts have been made to synthesize BiOCl, such as solvothermal method [13], spray drying method [14], hydrothermal method [15] and so on. However, these methods usually involve high temperature, high pressure, long reaction time and low efficiency. Solution combustion synthesis (SCS) is a method of synthesizing nanomaterials by using oxidation-reduction reaction among raw materials which is energy-efficient and time-

* Author to whom any correspondence should be addressed.

saving [16, 17]. Nevertheless, it is difficult for SCS to control the reaction process, and the powder products are easy to agglomerate. As a modification of SCS, Spray solution combustion synthesis (SSCS) can generate uniform spherical particles with relatively narrow size distributions, which is difficult to be accomplished by traditional SCS method [18]. Furthermore, SSCS can also well control the chemical uniformity of reactants and improve the dispersion of the product [18]. However, the reaction solution needs to be atomized into droplets and then be sprayed into the tube furnace for the combustion reaction, so the process time is longer than that of SCS. Up to now, many materials have been synthesized by SSCS. For instance, Du *et al* successfully synthesized hollow spherical MoO_3 photocatalyst by a facile one-step SSCS method [18]. Trusov *et al* reported that SSCS method is effective for the synthesis of spherical hollow particles of metals (Ni, Cu) [19]. Chen *et al* proposed that nanocrystalline indium tin oxide (ITO) powders were prepared by a novel spray combustion method [20].

In this work, we successfully synthesized novel BiOCl microspheres via a simple one-step SSCS method. The BiOCl microspheres, which are assembled by nanocrystals (10–20 nm), present hollow and porous structure. Additionally, the SSCS BiOCl shows excellent photocatalytic performance, and the degradation performance for RhB reaches 98% in 60 min. And the differences between the two methods (SCS and SSCS) of synthesizing BiOCl were discussed in terms of structure, morphology and photocatalytic activity.

2. Experimental

2.1. Materials

Bismuth nitrate pentahydrate ($\text{Bi}(\text{NO}_3)_3 \cdot 5\text{H}_2\text{O}$), ammonium chloride (NH_4Cl), tartaric acid ($\text{C}_4\text{H}_6\text{O}_6$), glycine ($\text{C}_2\text{H}_5\text{NO}_2$), rhodamine B (RhB) were purchased from Aladdin Chemical Reagent Co., Ltd, China. And nitric acid (HNO_3) was purchased from Sinopharm Chemical Reagent Co., Ltd. All chemicals were analytical grade and used directly without further purification.

2.2. Sample preparations

BiOCl microspheres were synthesized via SSCS method. (1) 6 mmol $\text{Bi}(\text{NO}_3)_3 \cdot 5\text{H}_2\text{O}$, 6 mmol NH_4Cl , 4 mmol $\text{C}_2\text{H}_5\text{NO}_2$ and 4 mmol $\text{C}_4\text{H}_6\text{O}_6$ and 10 ml 4 M nitric acid were added into a 50 ml beaker to form a homogeneous and transparent solution on a magnetic heating plate; (2) The prepared solution was transferred to an ultrasonic atomizer and pushed into the tube furnace with 600 °C preheating in the form of spray droplets. (3) The spray droplets take place combustion reaction under the action of heating, and products are adsorbed on the other side of the quartz tube. When the prepared solution was completely injected into the tube furnace, the tube furnace began to cool down, and the reaction lasts for about 30 min. Finally, the products were collected on the right side of the quartz tube. In order to investigate the influence of fuel ratio, the amount of $\text{Bi}(\text{NO}_3)_3 \cdot 5\text{H}_2\text{O}$ and NH_4Cl and the ratio

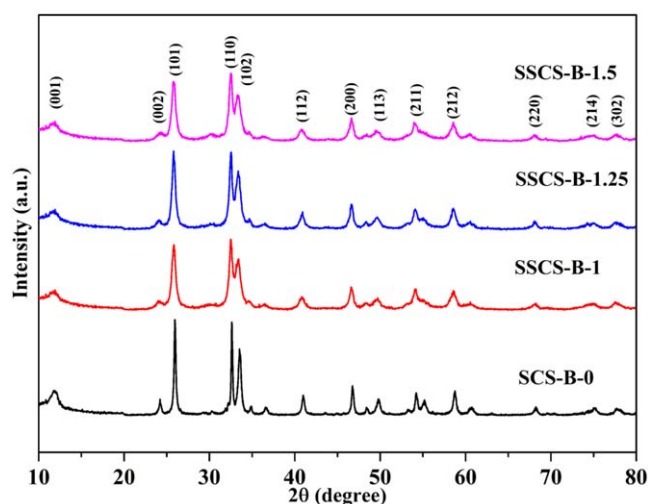


Figure 1. XRD patterns of as-prepared products.

of $\text{C}_2\text{H}_5\text{NO}_2$ and $\text{C}_4\text{H}_6\text{O}_6$ (1:1) were kept constant, while the amount of total fuel ($\text{C}_2\text{H}_5\text{NO}_2$ and $\text{C}_4\text{H}_6\text{O}_6$) was increased by 1.25 and 1.5 times respectively, and then the same steps were repeated. The farinose samples were obtained and labeled as SSCS-B-1, SSCS-B-1.25, and SSCS-B-1.5 according to the amount of fuel. For comparison, the sample called SCS-B-0 was prepared via traditional SCS route.

2.3. Characterization

The XRD patterns, SEM images, TEM images, BET data, DRS spectra, PL spectra and TOC determination were tested by x-ray diffraction (Bruker D8 Advance diffractometer), scanning electron microscopy (Quanta 250), high-resolution transmission electron microscopy (JEM-2100F, Japan), N_2 gas Brunauer–Emmett–Teller (BELSORP-max, Japan), ultraviolet–visible spectrophotometer (Shimadzu, Kyoto, Japan), photoluminescence spectrophotometer (FLS-980, UK) and total organic carbon (Tekemar Dohrmann, Apollo 9000) respectively.

2.4. Photocatalytic performance evaluation

The photodegradation property of the samples for the RhB degradation was monitored under visible light irradiation. In a typical procedure, 30 mg of catalyst and 30 ml of 20 mg l^{-1} aqueous RhB solution were added into a 50 ml quartz beaker. Then, the mixture was stirred in the dark for 30 min to obtain a good dispersion and sufficient adsorption–desorption equilibrium between the photocatalyst surface and RhB. After that, the suspensions were continuously stirred with 150 W halogen lamp under visible light irradiation, and the distance between the light source and the beaker was set at 20 cm. Finally, the concentration of RhB solution was evaluated by UV–vis spectrophotometer. The degradation efficiency was reported as $(1 - C/C_0)$. Here, C is the concentration of RhB solution after absorption and irradiation, while C_0 is initial concentration of RhB solution. To characterize the stability of as-synthesized power, five cycles of experiments were performed under the same conditions.

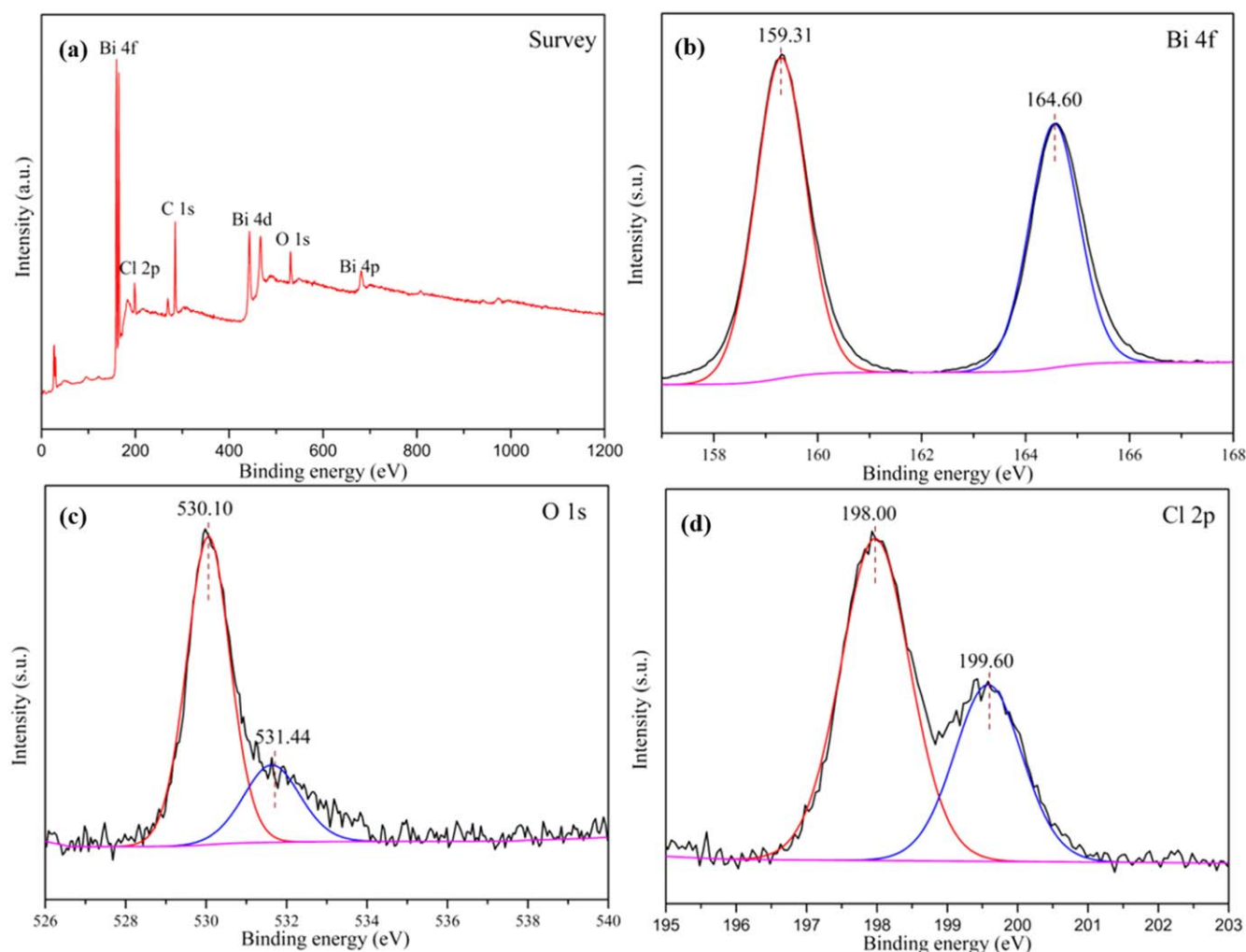


Figure 2. XPS spectra of (a) survey spectrum; (b) Bi 4f; (c) O 1s; and (d) Cl 2p for SSCS-B-1 sample.

3. Results and discussion

Figure 1 presents the XRD patterns of the as-obtained samples. It can be seen that all the diffraction peaks of as-synthesized products are indexed to tetragonal BiOCl (JCPDS card NO. 06-0249) with lattice constants of $a = b = 3.891 \text{ \AA}$ and $c = 7.369 \text{ \AA}$ [15]. The major XRD diffraction peaks at $2\theta = 25.86^\circ$, 32.49° and 33.45° corresponding to the (101), (110) and (102) planes, respectively. And these results show that BiOCl was successfully synthesized by SCS and SSCS. Based on the XRD patterns, the calculated grain size of the sample SCS-B-0, SSCS-B-X ($X = 1, 1.25, 1.5$) is 102.1 nm, 18.8 nm, 20.6 nm and 23.7 nm, respectively. These results indicate that SSCS could effectively control the grain size of the combustion products in comparison with SCS.

The detailed elemental composition and chemical state of the SSCS-B-1 sample, as shown in figure 2, was identified through XPS analysis. The XPS spectra were corrected for specimen charging by referencing the C 1s peak at 284.50 eV [21]. Figure 2(a) shows the survey spectrum of the SSCS-B-1 which presented the peaks of Bi, O, C and Cl elements. No peaks of other elements are found, indicating the SSCS-B-1 sample have a very high purity. The spectrum of Bi 4f

(figure 2(b)) for SSCS-B-1 shows two peaks which located at 159.31 and 164.60 eV, corresponding to Bi 4f_{7/2} and Bi 4f_{5/2} of Bi³⁺ [21], respectively. The spectra of O 1s is shown in figure 2(c), the peak at 530.10 eV coincides with the binding energy of bismuth–oxygen of BiOCl, the peak at 531.44 eV is assigned to the oxygen adsorbed by the BiOCl [22]. Figure 2(d) indicate that the Cl 2p XPS spectra with two peaks at 198.00 and 199.60 eV, which belongs to Cl 2p_{3/2} and Cl 2p_{1/2}, respectively [23]. The above results demonstrate BiOCl was successfully prepared by SSCS.

The microstructure construction of as-prepared samples was illustrated by SEM, TEM and HRTEM in figures 3 and 4. As shown in figure 3(a), the SCS product is composed of yellow powders, while the SSCS products turn into faint yellow and fluffy powders (figures 3(d), (g) and (j)). Figures 3(b) and (c) reveal that SCS BiOCl shows an irregular structure from agglomeration of nanorods and nanoparticles. However, all the samples obtained via SSCS present the morphology of uniformly dispersed microspheres. As shown in figure 3(e) and inset, SSCS-B-1 exhibits a structure of microspheres with a spherical shell thickness of a single layer nanocrystals and there is no stacking of nanocrystals. Figure 3(f) indicates that hollow microspheres are assembled

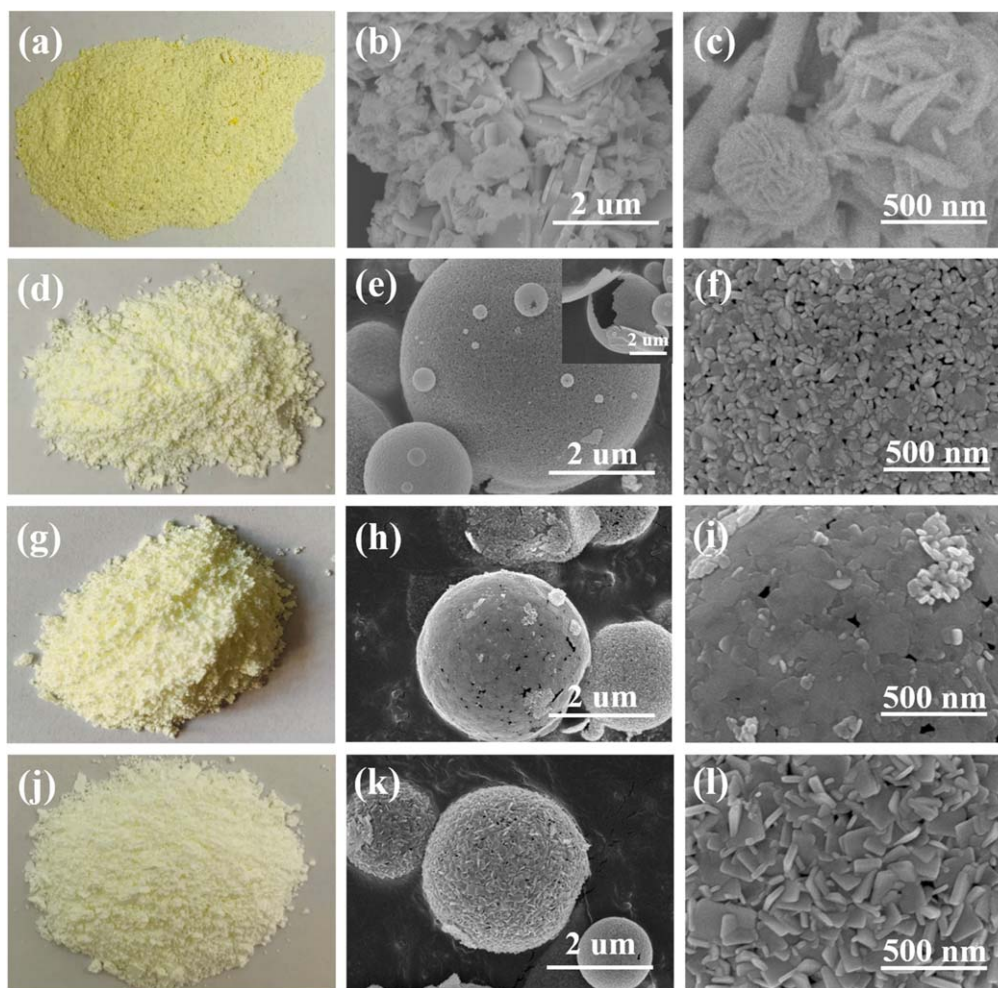


Figure 3. The macrophotographs and SEM images of as-prepared samples: (a)–(c) SCS-B-0; (d)–(f) SSCS-B-1; (g)–(i) SCS-B-1.25; (j)–(l) SSCS-B-1.5.

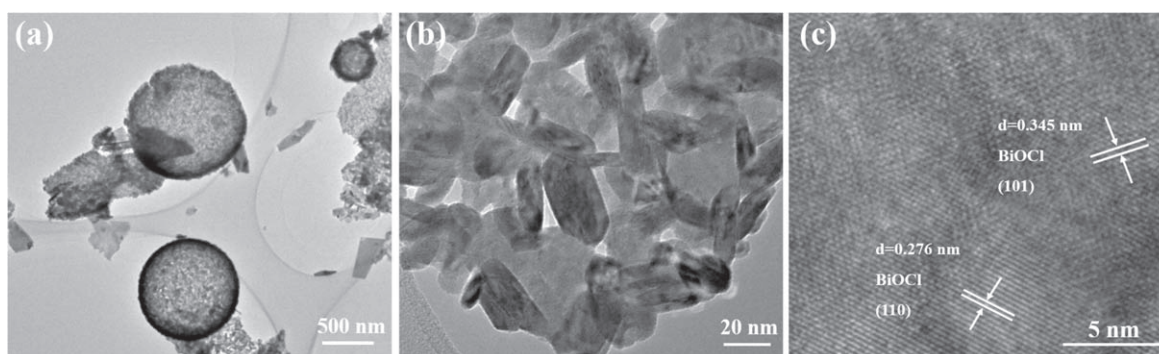


Figure 4. (a), (b)TEM images and (c) HRTEM image of SSCS-B-1.

by nanocrystals (10–20 nm) and there are a large number of uniform nanopores around the nanocrystals, which may help narrowing the band gap of BiOCl. The hollow porous structure retains the high specific surface area of nanocrystals. When the amount of fuel increases to 1.25 times (figures 3(h) and (j)), the surface of some microspheres is surrounded by a layer of film, which may be attributed to the increase in heat release. Figures 3(k) and (l) show that when the amount of

fuel increases to 1.5 times, the structures of the surface of some BiOCl microspheres change from nanoparticles to nanosheets. Figure 4 show the TEM and HRTEM images of SSCS-B-1 sample. Figure 4(a) further reveals that the BiOCl microspheres are hollow and porous. As shown in figure 4(b), the surface of BiOCl microspheres are composed of nanocrystals with the size of 10–20 nm, corresponding well to the calculated particles size. The HRTEM image of SSCS-B-1 is

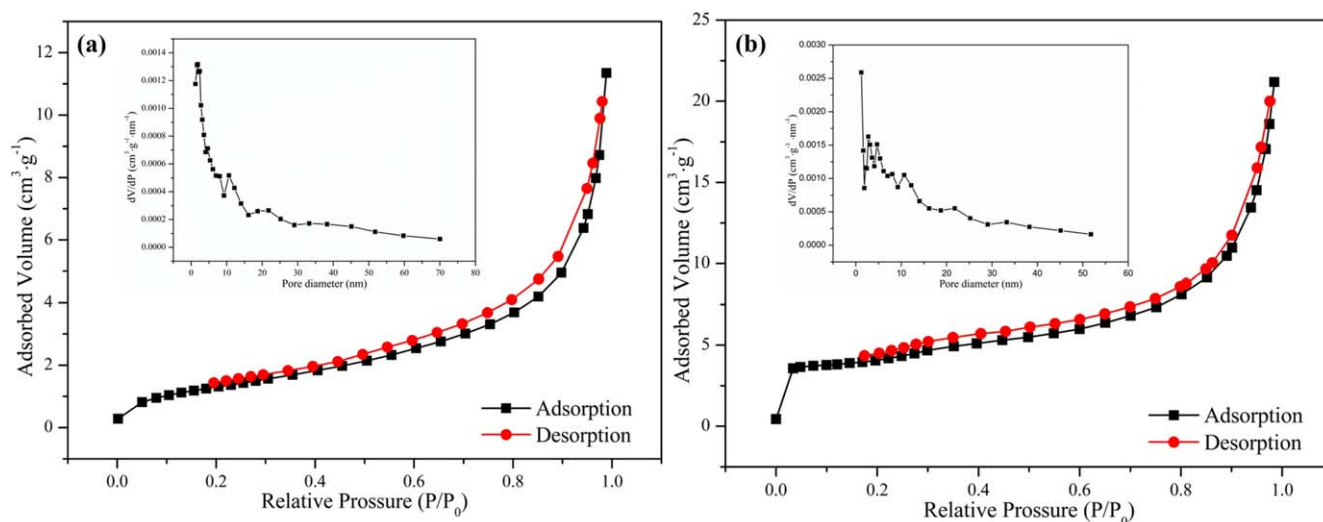


Figure 5. N_2 adsorption–desorption isotherms and the relevant pore-size distributions (insert) of (a) SCS-B-0 and (b) SSCS-B-1.

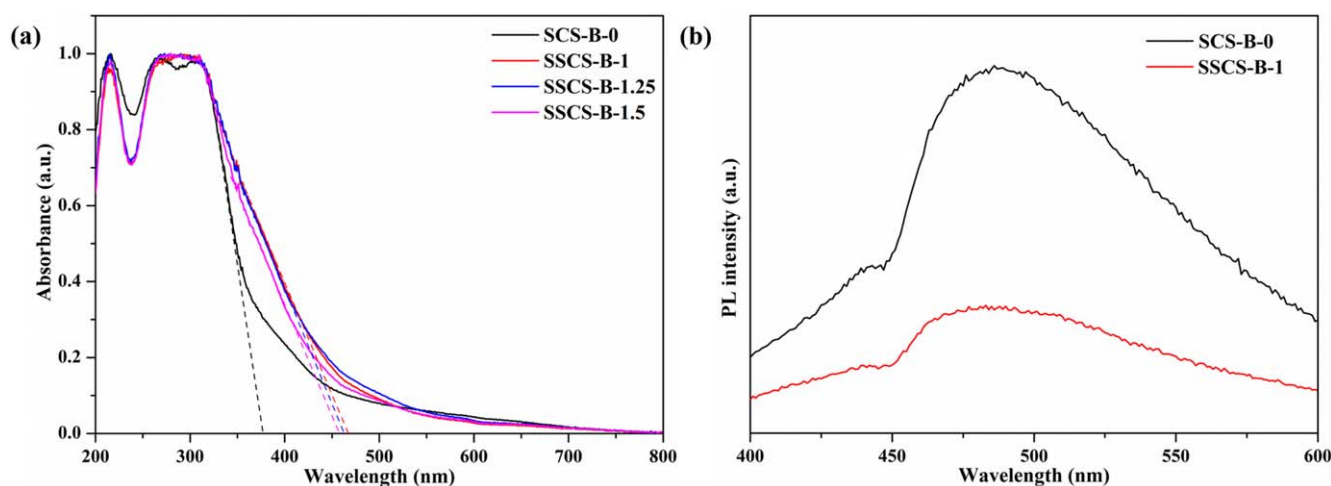


Figure 6. (a) UV–vis diffuse reflectance spectra of as-obtained samples; (b) PL spectra of SCS-B-0 sample and SSCS-B-1 sample.

Table 1. BET surface areas and average pore diameters of SCS-B-0 and SSCS-B-1.

| Sample | BET surface area ($m^2 \cdot g^{-1}$) | Average pore diameters (nm) | Total pore volume ($cm^3 \cdot g^{-1}$) |
|----------|---|-----------------------------|---|
| SCS-B-0 | 5.11 | 13.74 | 0.017 |
| SSCS-B-1 | 15.33 | 8.55 | 0.033 |

shown in figure 4(c), the lattice spacing of 0.276 nm, 0.345 nm can be obviously observed corresponding to the (110), (101) crystal planes of BiOCl, respectively. The result further demonstrates that high crystallinity BiOCl microspheres have been successfully prepared via SSCS route.

As shown in table 1 and figure 5, the BET surface areas of SCS-B-0 and SSCS-B-1 were calculated to be 5.11 and 15.33 $m^2 g^{-1}$, respectively, and the corresponding average pore diameters were 13.74 and 8.55 nm, respectively. And the average pore diameters of SSCS-B-1 are consistent with the results of TEM. Moreover, the total pore volume of SSCS-B-1 have a significant increase in comparison with SSCS-B-0.

Obviously, SSCS-B-1 sample prepared in SSCS method exhibits a larger specific surface area about three times and a smaller porous structure than that of SCS. The hollow porous BiOCl microspheres are assembled with single layer of nanocrystal, which not only helps retain the high surface area of nano crystal, but also avoids the agglomeration and stacking of nano crystal.

The UV–vis diffuse reflectance spectra of as-obtained samples were depicted in figure 6(a). In contrast to SCS BiOCl, SSCS BiOCl have a slight red-shift in the range of 350–500 nm. The band gaps of as-prepared samples are determined by the formula: $E_g = 1240/\lambda_g$ [24], in which E_g

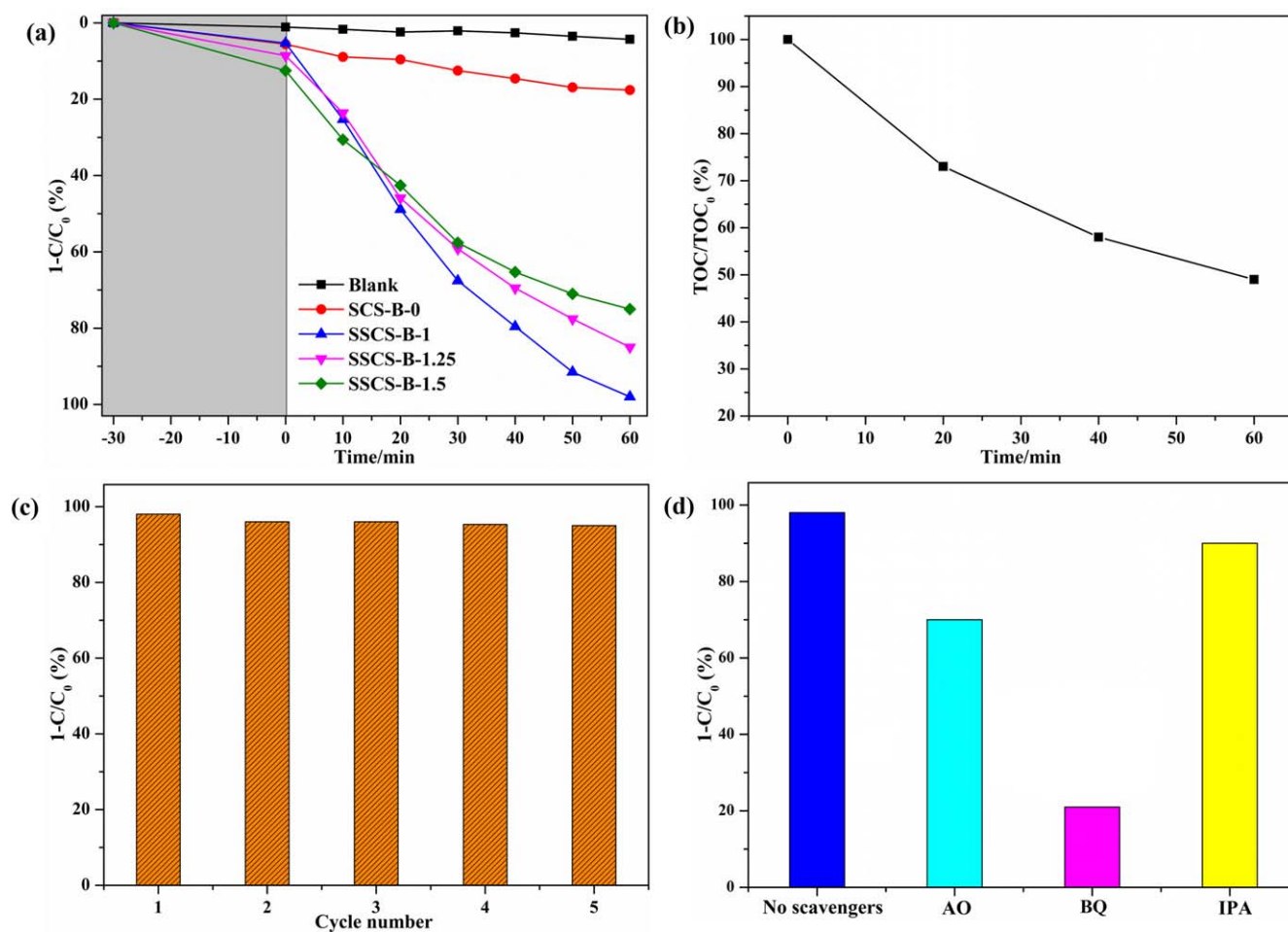


Figure 7. (a) Photocatalytic properties of as-synthesized samples; (b) TOC analysis of the RhB degraded with SSCS-B-1 sample under visible irradiation; (c) cyclic photodegradation of RhB for SSCS-B-1 sample; (d) the influence of different active species scavengers on photocatalytic performance of SSCS-B-1 sample.

and λ_g represent the band gap and wavelength, respectively. The calculated band gap of SCS-B-0, SSCS-B-1, SSCS-B-1.25 and SSCS-B-1.5 are approximately 3.29 eV, 2.71 eV, 2.68 eV and 2.66 eV, respectively. The results indicate that BiOCl prepared via SSCS method have a narrower band gap. Figure 6(b) shows photoluminescence (PL) spectra of SCS-B-0 and SSCS-B-1, in which PL spectra is related to the efficiency of the photogenerated electron-hole separation and the transfer behavior of charge carriers. As shown in figure 6(b), the PL spectra of the two samples exhibit an emission peak centered at 485 nm (~ 2.56 eV) under the excitation of 350 nm laser. And the PL intensity of SSCS-B-1 is significantly weaker than that of SCS-B-0, indicating that SSCS-B-1 enable the charge carriers to rapidly transfer onto the surface BiOCl microspheres. This facilitates the separation of photogenerated electrons and holes. The hollow porous structures of BiOCl microspheres with a large number of uniform holes in the shell could allow multiple scattering of UV-vis light, suggesting that the optical path length for light transporting through those BiOCl hollow structures are longer than that of the BiOCl nanoplates. Longer optical path length could increase the quantity of photogenerated electrons and holes

[25, 26]. Thus, the PL intensity of SSCS-B-1 microspheres tends to weaken and the band gap will become narrower. In addition, semiconductor nanomaterials exhibit size effect in the nano region, and the PL intensity of BiOCl weakens with the decrease of grain size [26, 27].

The photocatalytic performance investigations of the as-synthesized samples were probed by degrading rhodamine (RhB) under visible light illumination. As depicted in figure 7(a), RhB was almost not degraded without any photocatalyst under visible light illumination. SCS-B-0 sample exhibited a poor photocatalytic efficiency (18% in 60 min) for RhB degradation. However, SSCS-B-X ($X = 1, 1.25, 1.5$) samples show remarkably enhanced photocatalytic abilities in comparison with SCS-B-0 sample, which is mainly due to the following reasons: (1) hollow porous microspheres retain high specific surface area of nanocrystals and avoid the agglomeration of nanocrystal. (2) The uniformly distributed nanopores are conducive to the transport of reactants which can also provide sufficient active sites inside the microspheres. Furthermore, the photocatalytic performance of the SSCS samples gradually descends with the amount of fuel. Especially for SSCS-B-1 sample, near 98% removal rate can

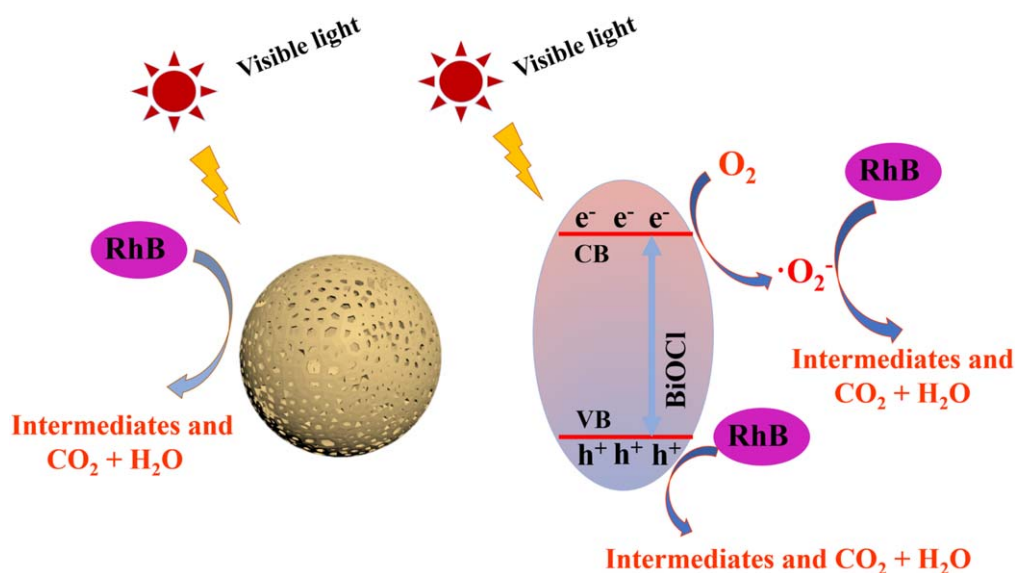


Figure 8. Photocatalytic mechanism of degrading RhB for BiOCl under visible light irradiation.

be achieved for RhB. To confirm the degraded substance, a TOC analytical experiment was carried out. As is shown in figure 7(b), 51% of the organic carbon is mineralized after 60 min of illumination. The result indicates some of the degradation intermediates produced in the photodegradation process still exist [10, 28, 29]. The photostability of the photocatalyst was conducted by cyclic photodegradation of RhB. As shown in figure 7(c), the photocatalytic performance after five cycles does not have significant decrease for SSCS-B-1 sample which demonstrates an excellent photostability.

To investigate the active species generated in the photocatalytic process, hydroxyl radicals ($\cdot\text{OH}$), superoxide radicals ($\cdot\text{O}_2^-$), and holes (h^+) were captured by isopropyl alcohol (IPA) [30], 1,4-benzoquinone (BQ) [31], and ammonium oxalate (AO) [32], respectively. The procedure similar to the above photocatalytic experiments in addition to adding 1 mM trapping agents. As depicted in figure 7(d), without adding scavengers, the degradation efficiency of RhB can reach 98%. When IPA served as trapping agent, the photocatalytic performance slightly declines, which demonstrates $\cdot\text{OH}$ is not the main active species in the degradation process. When AO was added, the photodegradation rate of RhB decreased obviously to 70%, indicating that h^+ specie plays the major roles in the RhB photocatalytic degradation. Nevertheless, the photodegradation rate dramatically decreased to 21% after adding BQ as trapping agent, which prove that $\cdot\text{O}_2^-$ is the most active specie for the photocatalytic degradation of RhB.

Based on the aforementioned analysis, the photocatalytic mechanism of BiOCl microspheres prepared via SSCS for the photocatalytic degradation of RhB is put forward in figure 8. Under visible light irradiation, BiOCl can be excited to produce photogenerated electron-hole due to the narrow band gap of it. The photogenerated electrons in the conduction band can react with the adsorbed O_2 form $\cdot\text{O}_2^-$ species. The reactive oxygen radical ($\cdot\text{O}_2^-$) and holes (h^+) can degrade

RhB to form intermediates, CO_2 and H_2O in the photocatalytic reaction.

4. Conclusions

In this work, hollow porous microspheres assembled by single layer of BiOCl nanocrystals were prepared successfully through a novel spray solution combustion method. The SEM and TEM results indicate that BiOCl obtained by SSCS method is self-assembled by nanoparticles to form hollow porous microspheres. Moreover, compared with BiOCl synthesized via SCS method, SSCS BiOCl microspheres have larger specific surface areas ($15.33 \text{ m}^2 \text{ g}^{-1}$) and narrower band gaps (2.66–2.71 eV), which can improve the absorption ability of BiOCl for visible light and further enhance the photocatalytic activity of BiOCl. A photocatalytic mechanism for hollow porous BiOCl microspheres is proposed, and $\cdot\text{O}_2^-$ and h^+ are the main active species in degrading RhB. The present research provides a method to prepare novel BiOCl microspheres with enhanced visible photocatalytic properties.

Acknowledgments

This work was supported by the Fundamental Research Funds for the Central Universities (2019ZDPY20).

Data availability statement

All data that support the findings of this study are included within the article (and any supplementary files).

ORCID iDs

Xiaohong Wang  <https://orcid.org/0000-0001-7391-3263>

References

- [1] Cheng S 2003 Heavy metal pollution in China: origin, pattern and control *Environ. Sci. Pollut. Res.* **10** 192–8
- [2] Yang Q, Zhai Y, Xu T, Zhao K and Li H 2019 Facile fabrication of Sc-BiOBr photocatalyst immobilized on palm bark with enhanced visible light photocatalytic performance for estradiol degradation *J. Phys. Chem. Solids* **130** 127–35
- [3] Jia C, Chen H S and Yang P 2018 Construction of hollow waxberry-like rutile-ianatase-TiO₂/SnO₂ towards enhanced photocatalysis *J. Ind. Eng. Chem.* **58** 278–89
- [4] Meng S, Li D, Fu X and Fu X 2015 Integrating photonic bandgaps with surface plasmon resonance for the enhancement of visible-light photocatalytic performance *J. Mater. Chem.* **3** 23501–11
- [5] Skiker R, Zourai M, Saidi M and Ziat K 2018 Facile coprecipitation synthesis of novel Bi₁₂TiO₂₀/BiFeO₃ heterostructure serie with enhanced photocatalytic activity for removal of methyl orange from water *J. Phys. Chem. Solids* **119** 265–75
- [6] Wang J, Zhang Z, Wang X, Shen Y, Guo Y, Wong P K and Bai R 2018 Synthesis of novel p–n heterojunction m-Bi₂O₄/BiOCl nanocomposite with excellent photocatalytic activity through ion-etching method *Chin. J. Catal.* **39** 1792–803
- [7] Li J, Li H, Zhan G M and Zhang L Z 2017 Solar water splitting and nitrogen fixation with layered bismuth oxyhalides SACC *Chem. Res.* **50** 112–21
- [8] Wu S, Wang C and Cui Y 2014 Controllable growth of BiOCl film with high percentage of exposed {001} facets *Appl. Surf. Sci.* **289** 266–73
- [9] Ye L, Su Y, Jin X, Xie H and Zhang C 2014 Recent advances in BiO_x (X = Cl, Br and I) photocatalysts: synthesis, modification, facet effects and mechanisms *Environ. Sci. Nano* **1** 90–112
- [10] Tian Y, Wu Q, Ma L, Liu X, Zhou C, Yang C, Tian T and Tian X 2017 Hierarchical BiOCl hollow microspheres assembled by ultrathin nanosheets with large surface area for the exceptional visible light photocatalytic activity *J. Nanosci. Nanotechnol.* **17** 6337–46
- [11] Yan X et al 2019 *In situ* synthesis of BiOCl nanosheets on three-dimensional hierarchical structures for efficient photocatalysis under visible light *Nanoscale* **11** 10203–8
- [12] Mera A C, Rodríguez C A, Pizarro-Castillo L, Meléndrez M F and Valdés H 2020 Effect of temperature and reaction time during solvothermal synthesis of BiOCl on microspheres formation: implications in the photocatalytic oxidation of gallic acid under simulated solar radiation *J. Sol-Gel Sci. Technol.* **95** 146–56
- [13] Zheng Y et al 2019 Binary solvent controllable synthesis of BiOCl towards enhanced photocatalytic activity *J. Phys. Chem. Solids* **135** 109–19
- [14] Su X, Hou L, Xia L, Yu X, Guo J, Zhu Y and Zhang Y 2019 Citric acid-modulated *in situ* synthesis of 3D hierarchical Bi@BiOCl microsphere photocatalysts with enhanced photocatalytic performance *J. Mater. Sci.* **54** 4559–72
- [15] Sarihi F T H A, Almarzouqi F, Kuvarega A T, Karthikeyan S and Selvaraj R 2020 Easy conversion of BiOCl plates to flowers like structure to enhance the photocatalytic degradation of endocrine disrupting compounds *Mater. Res. Express* **6** 125537
- [16] Gao M, Zhang D, Pu X, Li M, Yu Y M, Shim J J, Cai P, Kim S and Seo H J 2015 Combustion synthesis of BiOCl with tunable percentage of exposed {001} facets and enhanced photocatalytic properties *J. Am. Ceram. Soc.* **98** 1515–9
- [17] Mukasyan A S, Rogachev A S and Aruna S T 2015 Combustion synthesis in nanostructured reactive systems *Adv. Powder Technol.* **26** 954–76
- [18] Du X N, Wang X H, Liu Y and Feng P Z 2019 Spray solution combustion synthesis of hollow porous MoO₃ photocatalyst *Ceram. Int.* **45** 12599–601
- [19] Trusov G G, Tarasov A A, Goodilin E A, Rogachev A S, Roslyakov S, Rouvimov S, Podbolotov K and Mukasyan A S 2016 Spray solution combustion synthesis of metallic hollow microspheres *J. Phys. Chem. C* **120** 7165–71
- [20] Chen Z, Zhu Y, Duan Q, Chen A and Tang Z 2019 Spray-combustion synthesis of indium tin oxide nanopowder *J. Am. Ceram. Soc.* **102** 42–7
- [21] Cheng G, Xiong J and Stadler F J 2013 Facile template-free and fast refluxing synthesis of 3D desertrose-like BiOCl nanoarchitectures with superior photocatalytic activity *New J. Chem.* **37** 3207–13
- [22] Ding L, Wei R, Chen H, Hu J and Li J 2015 Controllable synthesis of highly active BiOCl hierarchical microsphere self-assembled by nanosheets with tunable thickness *Appl. Catal. B* **172** 91–9
- [23] Song Z, Dong X, Wang N, Zhu L, Luo Z, Fang J and Xiong C 2017 Efficient photocatalytic defluorination of perfluorooctanoic acid over BiOCl nanosheets via a hole direct oxidation mechanism *Chem. Eng. J.* **317** 925–34
- [24] Liu Y S, Quan B, Ji G B and Zhang H Q 2016 One-step synthesis of Ti³⁺ doped TiO₂ single anatase crystals with enhanced photocatalytic activity towards degradation of methylene blue *Mater. Lett.* **162** 138–41
- [25] Peng S, Li L, Zhu P, Wu Y, Srinivasan M, Mhaisalkar S, Ramakrishna S and Yan Q 2013 Controlled synthesis of BiOCl hierarchical self-assemblies with highly efficient photocatalytic properties *Chem. Asian J.* **8** 258–68
- [26] Zhang L, Wang W, Zhou L and Xu H 2007 Bi₂WO₆ nano- and microstructures: shape control and associated visible-light-driven photocatalytic activities *Small* **3** 1618–25
- [27] Roduner E 2006 Size matters: why nanomaterials are different *Chem. Soc. Rev.* **35** 583–92
- [28] Lei P, Chen C, Yang J, Ma W, Zhao J and Zhang L 2005 Degradation of dye pollutants by immobilized polyoxometalate with H₂O₂ under visible-light irradiation *Environ. Sci. Technol.* **39** 8466–74
- [29] Zainal Z, Lee C, Hussein M, Kassim A and Yusof N 2007 Electrochemical-assisted photodegradation of mixed dye and textile effluents using TiO₂ thin films *J. Hazard. Mater.* **46** 73–80
- [30] Gadhi A T, Hernández A G, Bizarro M, Jagdale P, Tagliaferro A and Rodil S E 2016 Efficient α/β -Bi₂O₃ composite for the sequential photodegradation of two-dyes mixture *Ceram. Int.* **42** 13065–73
- [31] Huang Y, Kang S, Yang Y, Qin H, Ni Z, Yang S and Li X 2016 Facile synthesis of Bi/Bi₂WO₆ nanocomposites with enhanced photocatalytic activity under visible light *Appl. Catal. B* **196** 89–99
- [32] Xiao X, Hu R, Tu S, Zheng C, Zhong H and Nan J 2015 One-pot synthesis of micro/nano structured β -Bi₂O₃ with tunable morphology for highly efficient photocatalytic degradation of methylparaben under visible-light irradiation *Rsc Advances* **5** 38373–81